



HAL
open science

A data-driven metamodel-based approach for point force localization

Mathieu Aucejo

► **To cite this version:**

Mathieu Aucejo. A data-driven metamodel-based approach for point force localization. *Mechanical Systems and Signal Processing*, 2022, 171, pp.108881. 10.1016/j.ymssp.2022.108881 . hal-03557526

HAL Id: hal-03557526

<https://hal.science/hal-03557526>

Submitted on 4 Feb 2022

HAL is a multi-disciplinary open access archive for the deposit and dissemination of scientific research documents, whether they are published or not. The documents may come from teaching and research institutions in France or abroad, or from public or private research centers.

L'archive ouverte pluridisciplinaire **HAL**, est destinée au dépôt et à la diffusion de documents scientifiques de niveau recherche, publiés ou non, émanant des établissements d'enseignement et de recherche français ou étrangers, des laboratoires publics ou privés.

A data-driven metamodel-based approach for point force localization

M. Aucejo^a

^aLaboratoire de Mécanique des Structures et des Systèmes Couplés, Conservatoire National des Arts et Métiers, 2 Rue Conté, 75003 Paris, France

Abstract

This paper introduces a novel strategy for point force localization in the frequency domain, based on metamodeling techniques and independent of the excitation level. More precisely, the ability of well-established techniques, such as Polynomial Chaos expansion or Universal Kriging, in providing accurate surrogate models for locating a point force through an optimization procedure is evaluated. The proposed methodology is applied in a purely data-driven context. Obtained results highlight the good performance of the proposed strategy for relatively small data sets, as well as its robustness to noise in both training and deployment phases.

Keywords: Force localization, Meta-modeling, Surrogate model, Model-based strategy, Data-driven approach.

1. Introduction

Force identification is an important research field in the structural mechanics community, since it is at the core of several engineering domains such as structural health monitoring or mechanical design of structures. Generally,

*Corresponding author. E-mail address: mathieu.aucejo@lecnam.net

the problem consists in locating and/or quantifying the excitation sources causing the vibration field measured by a set of sensors distributed over a structure. It results that force identification problems can be addressed by considering the localization and the quantification problems separately or as a whole. If we restrict ourselves to point source excitations, a rapid analysis of the dedicated literature reveals a wide variety of possible approaches to solve the three types of inverse problems above-mentioned.

When both the location and the evolution of a point force, i.e. its time history or its spectrum, are to be jointly estimated, several strategies can be implemented. Among the most widely used approaches, one can cite Tikhonov-like regularization [1–4], Kalman-type filtering [5, 6] or methods exploiting directly the equation of motion of the considered structure, such as the Force Analysis Technique [7–9] or the Virtual Field Method [10, 11]. Apart from the methods cited above, original nested techniques have also been proposed. They basically relies on the sequential application of the Tikhonov regularization and a dedicated localization procedure until convergence of the whole iterative process [12, 13]. It is eventually worth mentioning methods based on the identification of the modal participation factors, that efficiently solve the force reconstruction problem provided that the structure is linear and time invariant [14–16].

In situations where the location of the point forces is known a priori or the severity of an impact is sought, we are faced to a quantification problem, meaning that the reconstruction of the excitation signal or its energy level is the primary quantity of interest. In the first situation, the location of the point force being known, regularization strategies [17, 18] and Kalman-like

filtering [19, 20] can be directly implemented, since the only noticeable difference with the joint estimation problem (localization and quantification) lies in the size of the mathematical system to deal with. In the second case, where only the excitation level is required to assess the severity of an impact event, learning strategies based on neural networks have been proposed to efficiently perform this task [21–24].

Finally, the last problem encountered in the field of force identification is the localization of a point force from vibration data. The specificity of this inverse problem is that the point force amplitude is generally unknown. That is why, methods based on the information provided by the measured data only have been developed. From a very general standpoint, they mainly belong to the class of triangulation strategies. Among the latter, one can cite the methods based on wave propagation models [25–29], super-resolution approaches [22, 30] or learning/metamodeling techniques [21, 23, 24, 31–34]. Metamodeling is commonly used in structural mechanics for multiparameter optimization or uncertainty quantification, since they provide a surrogate model whose instances are generally less expensive than those of the original computational model. Although they appeared more than eighty years ago, their application has really started to spread in the last three decades, thanks to the increase in the computing resources. When focusing the literature review on force localization problems, which is the core of this paper, one can note that metamodeling approaches, such as artificial and convolutional neural networks, have gained in popularity over the last twenty years, especially in the field of structural health monitoring [21, 23, 35–38]. However, other strategies, such as Polynomial Chaos Expansion or Universal Kriging, which

are well-established methods in structural mechanics, have apparently not been fully exploited. Their suitability for solving data-driven machine learning regression problems has only been demonstrated in 2019 by Torre et al. [39], paving the way for various applications in the context of force identification. Actually, the first application of such metamodeling techniques has been proposed very recently by Seno and Aliabadi in the context of Structural Health Monitoring [40]. They propose to apply Ordinary Kriging for locating impact forces from the time of arrival of the Lamb waves measured on a composite structure¹.

Following the idea of Torre et al., the present paper introduces a novel data-driven strategy for locating point forces in the frequency domain. The proposed method relies on an optimization procedure taking advantage of the metamodeling techniques commonly employed in computational mechanics to perform the localization. More precisely, this contribution aims at evaluating the ability of Polynomial Chaos Expansion (PCE) and Universal Kriging (UK) in providing accurate surrogate models for solving point force localization problems. To this end, the paper is organized as follows. Section 2 introduces the general architecture of the localization procedure as well as the related theoretical ingredients. In section 3, the localization strategy is applied in a purely numerical context in order to assess the robustness of the proposed approach with respect to various parameters, such as the mea-

¹It is worth mentioning, that this work has been published short before the initial submission of this paper. The author was not aware of the work of Seno and Aliabadi when writing and submitting the paper.

surement noise, the sensor configuration, the frequency range of interest or the size of training data set. It should be mentioned that such a parametric and systematic study is rarely presented in the literature, essentially for the sake of conciseness. As shown in this section, obtained results allows defining some guidelines in the design decision process, while providing further insights into the behavior of the proposed strategy in various conditions. Finally, a real-world experiment is carried out in section 4 to appraise the localization performances of the present methodology in operating conditions.

Considering the existing literature, the main contributions or salient points of this paper are:

- The application of PCE and UK to point force localization problem in the frequency domain using a two-step strategy;
- The construction of training, validation and testing datasets adapted to the specificities of the problem and the metamodeling strategies considered;
- The proposed strategy only relies on the vibration spectra measured by a set of sensors and no particular feature extraction is required;
- A careful and thorough parametric study of the design parameters of an experiment (such as the sensors quality, the number and location of the sensors or the size of the training data set);
- The determination of general guidelines to facilitate the design decision process.

2. Localization strategy

This section intends to introduce the general ideas behind the proposed data-driven localization strategy. More precisely, a general overview of the present approach is first given in order to define its main architecture. Then, each building block of the method is detailed in a dedicated part to make the paper self-contained and give the reader all the necessary information to implement the method. As for the notation system, classical notations are used, namely, bold characters for vectors or vector-valued functions and normal font for scalars or scalar-valued functions.

2.1. General overview

The proposed strategy is a metamodel-based approach, which aims at locating point force excitations acting on linear and time-invariant structures in the frequency domain. In this regards, its general architecture, defined in Fig. 1, is divided, as for any data-driven strategy, into two distinct stages: a training phase and a deployment phase.

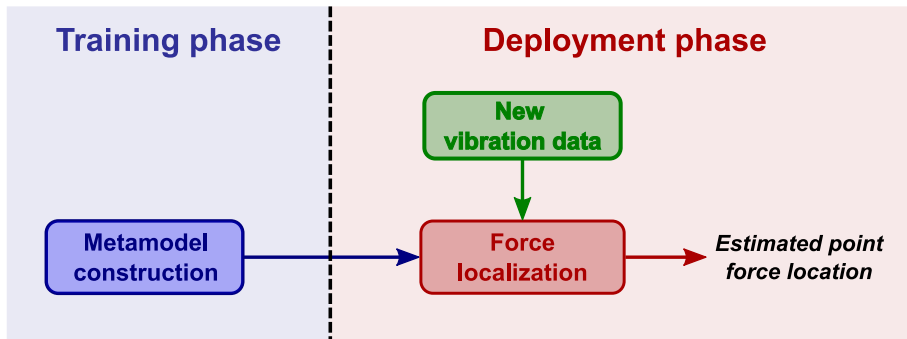


Figure 1: Basic workflow of the localization strategy

The training phase aims at creating an accurate metamodel of the considered system based on the vibration data collected on a given set of sensors resulting from a point force excited the structure at various locations. The deployment phase consists in exploiting the metamodel in order to estimate, through an optimization procedure, the point force location from new vibration data, i.e. from data not used for training the metamodel. For the sake of clarity, the practical organization of each phase is proposed in the next subsections to properly introduce the related theoretical elements.

2.2. Training phase – Metamodel construction

By definition, a metamodel, a.k.a. surrogate model, is a model of a possibly unknown model, built from a training data set, related some input parameters \mathbf{x} to some quantities of interest \mathbf{y} . Basically, a metamodel \mathcal{M} aims at approximating the mapping between the input parameters and the quantities of interest from the relation:

$$\mathbf{y} \approx \mathcal{M}(\mathbf{x}). \quad (1)$$

In the present paper, the input parameters \mathbf{x} are the point force coordinates, while the quantities of interest \mathbf{y} correspond to the vibration data (displacement, velocity or acceleration) measured by a set of sensors distributed over the structure considered.

As illustrated in Fig. 2, the construction of a model requires four basic steps: design of experiment, data generation and normalization, metamodel computation and validation. At the end of the process, a usable metamodel is obtained and can be used to generate inexpensive predictions of the vibration

responses for point force locations that have not been seen before. Because each step of the metamodel construction deserves a particular attention, a specific section is dedicated to each of them.

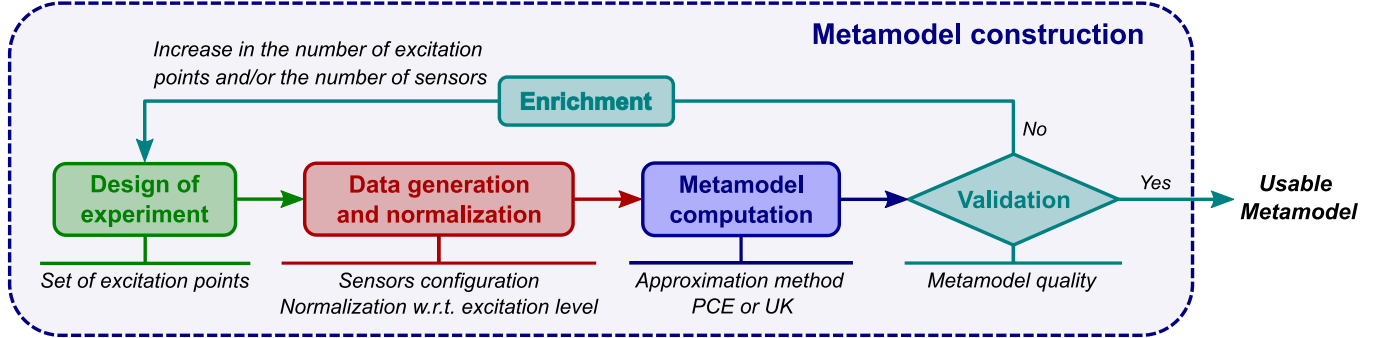


Figure 2: Training phase – Block diagram of the metamodel construction

2.2.1. Design of experiment

Any metamodel construction starts by the generation of sample points in the input parameters space. In the present application, the sample points correspond to a set excitation points. Their distribution over the structure is generally chosen to properly fill the input space. When the metamodel construction is based on a physical model, space-filling techniques, such as Latin Hypercube Sampling or low-discrepancy sequences (Halton, Hammersley or Sobol), can be used to generate samples that are reasonably uniformly distributed [41]. However, when the metamodel is build from experimental data, these methods can be hardly applied, essentially for practical reasons (materialization of the grid of excitation points, accessibility issues, ...). Instead, a common practice in force localization problems consists in using a regular grid [21, 23]. Following these considerations, it has been chosen to

define a set of n_e evenly-spaced excitation points, noted $\mathcal{X}_{\text{train}}$, to generate the corresponding vibration responses collected in the set $\mathcal{Y}_{\text{train}}$.

2.2.2. Data generation and normalization

Once the set $\mathcal{X}_{\text{train}}$, containing n_e excitation points, is defined, the set of the corresponding vibration responses $\mathcal{Y}_{\text{train}}$ can be generated. Practically, $\mathcal{Y}_{\text{train}}$ gathers the data measured (or computed from a calibrated numerical model) at n_f frequencies by a set of n_s sensors distributed over the structure, for each excitation point defined in $\mathcal{X}_{\text{train}}$. Unfortunately, the vibration responses can't be used directly to train the metamodel for two main reasons. First of all, most of the methods developed for building metamodels generally operate on real-valued data, whereas the vibration responses expressed in the frequency domain are inherently complex-valued data². To bypass this problem and enable the application of a wide range of metamodeling algorithms, a simple and classical solution consists in splitting the vibration measurements into real and imaginary parts. In doing so, the vector $\mathbf{y}(f_j, \mathbf{x}_k)$ corresponding to the vibration response measured by the n_s sensors at the frequency f_j , resulting from a force located at point \mathbf{x}_k , has $2n_s$ components³. Second, since the structures are supposed linear, the measured vibration levels are directly proportional to that of the excitation. In particular, this implies that the excitation level must theoretically be known, if one wants to obtain an accurate surrogate model. To make the localization method inde-

²This apparent limitation is mainly related to some of the algorithms used to compute the internal parameters of the metamodels.

³More precisely, the first n_s components (resp. the last n_s ones) are the real parts (resp. the imaginary parts) of the vibration measured by the n_s sensors.

pendent of the excitation level, the vibration responses must be normalized. To do so, each component of the vector $\mathbf{y}(f_j, \mathbf{x}_k)$ is divided by the Euclidean norm $\|\mathbf{y}(f_j, \mathbf{x}_k)\|_2$.

In the end, the set of vibration responses $\mathcal{Y}_{\text{train}}$, resulting from the transformations described above, is a collection of $n_e \times 2n_s \times n_f$ normalized real-valued data. Given this definition, an element of $\mathcal{Y}_{\text{train}}$ will consequently be noted $y_i(f_j, \mathbf{x}_k)$ for $i \in [1, 2n_s]$.

2.2.3. Metamodel computation

After defining the experimental design and generating the data, a training set $\mathcal{T} = (\mathcal{X}_{\text{train}}, \mathcal{Y}_{\text{train}})$ is available for building a metamodel. The existing literature is rich of metamodeling algorithms [42, 43] and comparing all these techniques is outside the scope of this paper. Here, it has been chosen to assess the ability of Polynomial Chaos expansion (PCE) and Universal Kriging (UK) in providing accurate surrogate models for solving point force localization problems. This particular choice has been made, because these methods are well-established in the structural mechanics community and have proved their efficiency for dealing with multiparameter optimization or uncertainty quantification problems.

When applying PCE or UK strategies, one has to keep in mind that these metamodeling techniques are MISO (Multiple-Inputs and Single-Output) approaches. It results that a metamodel should be at least computed for each component $i \in [1, 2n_s]$, that is:

$$y_i(f, \mathbf{x}) \approx \mathcal{M}_i(f, \mathbf{x}). \quad (2)$$

This approach implies the use of the whole training dataset at once. However, due to the necessary complexity of the model, such an approach leads to a substantial increase in the computation resources, and so in the computation time. That is why, it has been chosen, instead, to build one metamodel per component y_i and frequency f_j . It results that a total of $2n_s \times n_f$ independent metamodels is built. In doing so, one has more but simpler metamodels to compute (see section 2.4).

In the rest of this section, PCE and UK metamodeling techniques are briefly recalled, along with the main internal parameters used in the numerical and experimental applications carried out in sections 3 and 4. In the present contribution, their practical implementation relies on the UQLab toolbox [44].

Polynomial Chaos Expansion

PCE has been originally proposed by Wiener in a seminal paper published in 1938 [45]. Considering the input parameters \mathbf{x} , i.e. the unknown point force location, as a random vector with M independent components x_m , corresponding to the coordinates of the point force, PCE assumes, for any vibration response $y_i(f_j, \mathbf{x})$, the following spectral expansion [46]:

$$y_i(f_j, \mathbf{x}) \approx \sum_{p=0}^{P-1} \beta_p(f_j) \Psi_p(\mathbf{x}). \quad (3)$$

In the previous equation, P is the number of terms, $\beta_p(f_j)$ are the unknown deterministic coefficients, while $\Psi_p(\mathbf{x})$ are multivariate orthogonal polynomials. Because the components of \mathbf{x} are independent, $\Psi_p(\mathbf{x})$ can be expressed

as the tensor product of univariate orthogonal polynomials $\psi_m^{\alpha_m}$ of maximum degree d , that is:

$$\Psi_p(\mathbf{x}) = \prod_{m=1}^M \psi_m^{\alpha_m}(x_m) \text{ with } \alpha_m = 0, 1, \dots, d \text{ and } \sum_{m=1}^M \alpha_m \leq d. \quad (4)$$

The latter equation implies that the multivariate polynomials $\Psi_p(\mathbf{x})$ retained in the expansion have a total degree less than or equal to d . Accordingly, the total number of terms P in the PCE is equal to the binomial coefficient $C(M + d, d)$.

At this stage, it remains to choose the univariate polynomial family $\psi_m^{\alpha_m}$ associated to each input parameter x_m , to define the polynomial order d and to compute the expansion coefficients $\beta_p(f_j)$ to obtain a PCE adapted to the proposed localization strategy.

The univariate polynomial family is chosen according to the marginal probability distribution of the input parameters x_m , considered as random variables. Here, each point force location is considered equiprobable over the structure, which is a reasonable hypothesis in absence of any prior information. It is thus assumed that the point force coordinates x_m are uniformly distributed along the related axis. Following Askey and Wilson, the corresponding univariate polynomial family $\psi_m^{\alpha_m}$ is the Legendre polynomial family [47].

The definition of the polynomial order d for a particular application is far from an easy task, since the size of the basis is conditioned to that of the experimental design, while a sufficient number of elements is required to obtain an accurate metamodel. For this reason, it is often recommended to apply

a basis-adaptive strategy, that allows selecting a suitable basis by progressively increasing the maximum polynomial degree d and choosing the basis minimizing some generalization error [48]. For the applications presented in this paper, the optimal polynomial degree d is sought in the range [20, 50] because of the non linearity of $y_i(f_j, \mathbf{x})$ w.r.t. the point force location \mathbf{x} . Finally, several techniques can be implemented to compute the expansion coefficients $\beta_p(f_j)$, such as projection methods (Gaussian or Smolyak’s quadrature) or regression approaches (dense or sparse). In the present contribution, the sparse Least Angle Regression method has been adopted, because it is robust to noise and requires fewer design points n_e than basis functions P [39, 48].

Universal Kriging

Universal Kriging finds its roots in the original work of Krige in 1951 [49], although its theoretical developments are due to Matheron in the 1960s [50]. By definition, the Universal Kriging approximates the vibration response $y_i(f_j, \mathbf{x})$ as a sum of a global approximation $g_i(f_j, \mathbf{x})$, representing its trend, and a local approximation $l_i(f_j, \mathbf{x})$, describing the local variations of the function around $g_i(f_j, \mathbf{x})$. Consequently, the Universal Kriging model simply writes:

$$y_i(f_j, \mathbf{x}) \approx g_i(f_j, \mathbf{x}) + l_i(f_j, \mathbf{x}). \quad (5)$$

Because Universal Kriging is a Gaussian process modeling, $g_i(f_j, \mathbf{x})$ is the mean value of the Gaussian process, while $l_i(f_j, \mathbf{x})$ is related to its variance. From a general perspective, the function $l_i(f_j, \mathbf{x})$ is defined as weakly stationary stochastic process with zero mean $Z_i(f_j, \mathbf{x})$ and constant process variance

σ^2 , that is:

$$l_i(f_j, \mathbf{x}) = \sigma^2 Z_i(f_j, \mathbf{x}). \quad (6)$$

In the previous equation, the Gaussian process $Z_i(f_j, \mathbf{x})$ is characterized by its covariance function $R(\mathbf{x}, \mathbf{x}')$ measuring the correlation between two samples points x_m and x'_m of the design space. Furthermore, if the noise $n_i(f_j)$ corrupting the vibration data is considered as an additive white Gaussian noise process with variance σ_n^2 , then:

$$l_i(f_j, \mathbf{x}) = \sigma^2 Z_i(f_j, \mathbf{x}) + n_i(f_j), \quad (7)$$

is a zero-mean Gaussian process with covariance function $\Sigma(\mathbf{x}, \mathbf{x}') = \sigma^2 R(\mathbf{x}, \mathbf{x}') + \sigma_n^2 \delta_{\mathbf{x}\mathbf{x}'}$ (where $\delta_{\mathbf{x}\mathbf{x}'}$ is the Kronecker delta function).

It results from what follows that the general Universal Kriging model is given by:

$$y_i(f_j, \mathbf{x}) \approx g_i(f_j, \mathbf{x}) + \sigma^2 Z_i(f_j, \mathbf{x}) + n_i(f_j). \quad (8)$$

Eq. (8) shows that a Universal Kriging model is fully defined after selecting the trend $g_i(f_j, \mathbf{x})$ and the covariance function $R(\mathbf{x}, \mathbf{x}')$ and calculating all the unknown parameters, such as σ^2 and σ_n^2 , through optimization.

The choice of the trend is a crucial step in the definition of the Universal Kriging model, since it aims at capturing the global behavior of the function to approximate. Similarly to Eq. (3), it can generally be expressed as [51]:

$$g_i(f_j, \mathbf{x}) = \sum_{p=0}^{P-1} \beta_p(f_j) k_p(\mathbf{x}). \quad (9)$$

where $k_p(\mathbf{x})$ is a multivariate polynomial basis function. In this paper, two particular trends are considered: multivariate polynomial and Polynomial

Chaos trends. For the Polynomial Chaos trend, $k_p(\mathbf{x})$ is given by Eq. (4), while, for the multivariate polynomial trend, it is written:

$$k_p(\mathbf{x}) = \prod_{m=1}^M x_m^{\alpha_m} \text{ with } \alpha_m = 0, 1, \dots, d \text{ and } \sum_{m=1}^M \alpha_m \leq d, \quad (10)$$

where d is the maximum polynomial degree. As for the PCE, a basis-adaptivity strategy can be adopted to determine the adequate polynomial degree. Instead, a set of numerical experiments has been conducted by making varying d from 0 to 5 in order to find the polynomial degree leading to the best trade-off in terms of computational efficiency and localization accuracy. Based on this return on experience, a quadratic trend is chosen, meaning that $d = 2$. The resulting Universal Kriging formulations will be referred to as Polynomial Chaos Kriging (PCK) and Quadratic Trend Kriging (QTK) in the rest of the paper. It should be noted that the Polynomial Chaos trend has been implemented rather recently in the Universal Kriging framework, compared to the multivariate polynomial trend [52]. The basic motivation behind PCK is to obtain more accurate metamodels by combining the global approximation ability of PCE with the local interpolation property of Kriging⁴.

Regarding the choice of the correlation function $R(\mathbf{x}, \mathbf{x}')$, a separable structure is adopted, since the point force coordinates are supposed independent. This assumption leads to:

$$R(\mathbf{x}, \mathbf{x}') = \prod_{i=1}^M R_m(x_i, x'_i). \quad (11)$$

⁴For PCK, the orthogonal polynomial basis $\psi_m^{\alpha_m}$ and the interval defined to search the optimal polynomial degree d are the same as those used for building the PCE metamodel.

The literature is rich of correlation models for $R_m(x_m, x'_m)$, such as Gaussian or Matérn types, satisfying the Mercer’s conditions (continuous, symmetric and positive definite) [43]. In the present paper, the Matérn 3/2 correlation function has been chosen, because it provides metamodels robust to noisy training data⁵ [53]. Consequently, the correlation function $R_m(x_m, x'_m)$ is defined such that:

$$R_m(x_m, x'_m) = \left(1 + \frac{\sqrt{3}|x_m - x'_m|}{\ell_m}\right) \exp\left(-\frac{\sqrt{3}|x_m - x'_m|}{\ell_m}\right), \quad (12)$$

where ℓ_m is the strictly positive correlation length.

Finally, once the main ingredients of the Kriging model have been defined, it remains to compute the expansion coefficients $\beta_p(f_j)$, the variances σ^2 and σ_n^2 as well as the correlation lengths ℓ_m . Practically, all these quantities are computed through an optimization procedure. Here, we have opted for the cross-validation estimation method, which is the default option in UQLab [54].

2.2.4. Metamodel validation

To complete the training phase, it is important to evaluate the accuracy of the metamodel by estimating its generalization ability. In other words, it is intended to assess the performance of the metamodel on unseen data. This is generally a crucial step, since it provides a degree of confidence in the metamodel built previously. If a validation set $\mathcal{V} = (\mathcal{X}_{\text{val}}, \mathcal{Y}_{\text{val}})$ is available, the quality of the metamodel can be estimated from the predictivity

⁵Actually, the Matérn correlation functions yields to less smooth metamodels than those obtained with Gaussian kernels, which is often a more realistic assumption in many engineering applications.

coefficient Q_2 [55]. Here, a modified version of this indicator is proposed to evaluate the global accuracy of the set of $2n_s \times n_f$ metamodels built in the previous step. As a result, if \mathcal{X}_{val} is a collection of n'_e excitation points, then \mathcal{Y}_{val} has $n'_e \times 2n_s \times n_f$ elements and the global predictivity coefficient Q_2^g writes:

$$Q_2^g = 1 - \frac{n'_e - 1}{n'_e \cdot 2n_s \cdot n_f} \sum_{i=1}^{2n_s} \sum_{j=1}^{n_f} \left[\frac{\sum_{k=1}^{n'_e} (y_i(f_j, \mathbf{x}_k) - \widehat{y}_i(f_j, \mathbf{x}_k))^2}{\sum_{k=1}^{n'_e} (y_i(f_j, \mathbf{x}_k) - \mu_i(f_j))^2} \right], \quad (13)$$

where \mathbf{x}_k is an element of \mathcal{X}_{val} , $y_i(f_j, \mathbf{x}_k)$ is an element of \mathcal{Y}_{val} , $\widehat{y}_i(f_j, \mathbf{x}_k)$ is the corresponding value estimated by the metamodel and $\mu_i(f_j) = \frac{1}{n'_e} \sum_{k=1}^{n'_e} y_i(f_j, \mathbf{x}_k)$ is the sample mean over \mathcal{X}_{val} of the element (i, j) of \mathcal{Y}_{val} .

If the metamodels quality is judged poor, the metamodel construction can be enriched by increasing the number of excitation points n_e and/or the number of sensors n_s of the training set \mathcal{T} . In what follows, the quality of the metamodels is considered representative of the actual model and usable for localization purposes if $Q_2^g \geq 0.7^6$. In the applications presented in the rest of the paper, the value of the global predictivity coefficient is not given, except when it does not satisfy the validation requirement.

2.3. Deployment phase – Force localization

The deployment phase consists in integrating the metamodel into the force localization process. As illustrated in Fig. 3, the metamodel serves as

⁶This lower bound has been set on the basis of the results presented in section 3 and from another set of numerical experiments not presented in the present paper.

the basis for estimating an unknown point force location from a set normalized vibration data unseen during the training phase.

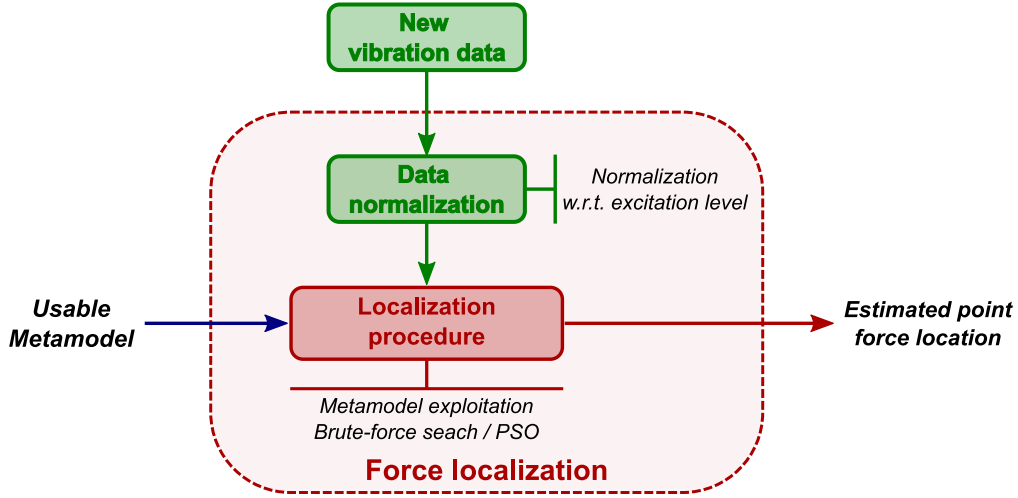


Figure 3: Deployment phase – Block diagram of the force localization procedure

Practically, the unknown point force location is sought as the solution of the following minimization problem:

$$\hat{\mathbf{x}} = \underset{\mathbf{x}}{\operatorname{argmin}} \frac{1}{2n_s \cdot n_f} \sum_{i=1}^{2n_s} \sum_{j=1}^{n_f} (y_i(f_j, \mathbf{x}) - \hat{y}_i(f_j, \mathbf{x}))^2, \quad (14)$$

where the notations used are the same as in Eq. (13).

In the present paper, two strategies are implemented to solve the previous minimization problem. The first one is the brute-force search. This approach is considered here, because the metamodel provides an almost inexpensive approximate of the vibration response for a given potential point force location. The latter property allows defining a dense search space to find the

actual point force location or at least define the possible excitation region. The second strategy consist in applying the Particle Swarm Optimization (PSO) technique, which is a metaheuristic optimization that has proved its suitability for solving force localization problems [56].

If a test set $\mathcal{S} = (\mathcal{X}_{\text{test}}, \mathcal{Y}_{\text{test}})$ is available, the localization performances of proposed methodology can be easily evaluated. To this end, an indicator, measuring the localization accuracy w.r.t. a characteristic dimension of the considered structure, is defined. For a particular point force location \mathbf{x}_t belonging to $\mathcal{X}_{\text{test}}$, the localization error ε_t is mathematically expressed as:

$$\varepsilon_t = \frac{d_t}{L_c}, \quad (15)$$

where $d_t = \|\widehat{\mathbf{x}}_t - \mathbf{x}_t\|_2$ is the Euclidean distance between the estimated and the actual point force location, $\widehat{\mathbf{x}}_t$ and \mathbf{x}_t respectively, while L_c is the characteristic length of the structure undergoing the excitation. For straight beams, L_c is the length, whereas for rectangular plates, it is chosen as the length of the diagonal.

From the localization error, several indicator can be derived such as the median value $\bar{\varepsilon}_t$, the 95% credible interval (CI), as well as the probability of good localization:

$$P_\gamma = P(\{\varepsilon_t \leq \gamma\}) = \frac{\text{card}(\{\varepsilon_t \leq \gamma\})}{n_e''}, \quad (16)$$

where γ is the target localization error and n_e'' is the number of point force locations in $\mathcal{X}_{\text{test}}$. In other words, P_γ is the probability of locating a point force within a tolerance γ .

2.4. Practical considerations

The proposed localization strategy, based on PCE or UK metamodels, differs from the other data-driven techniques, and more particularly from neural networks approaches, essentially in the design decision process. Indeed, although the general workflow is similar for all the data-driven/learning strategies, the construction of a representation model requires different levels of expertise depending on the method considered.

When neural networks is chosen as metamodeling technique, many design decisions have to be made. First, the general architecture of the network has to be defined. This implies the choice of the number of layers (shallow or deep network), their type (convolutional, recurrent, fully connected, normalization, etc.) and their width (i.e. the number of nodes in a specific layer)⁷. These decisions have an impact on the network complexity. The more complex the network is, the more it is prone to overfitting. To prevent this effect, some regularization techniques can be implemented such as ℓ_2 and ℓ_1 regularization, dropout, batch/layer normalization or early stopping. However, each regularization strategy is generally accompanied by a set of parameters that have to be tuned or learned during the training phase. Second, a training algorithm must be selected. The most widely used algorithms is the gradient descent and its variants (RMSprop, Adam, AdaBelief, etc.) that requires a proper choice a the learning rate parameter. When defining the optimizer,

⁷There exists no general rules for determining a priori an adequate architecture. To this end, automated search techniques can be employed for testing different network configurations.

one also has to define the loss function to minimize, the number of epochs and/or a convergence criterion and the size of the mini-batches, if any.

On the contrary, the proposed approach requires less design decisions. Indeed, the design process is generally limited to the choice of the type of the metamodel (PCE or UK), the definition of the order of the polynomial expansion and the computation and the tuning of the parameters and hyperparameters associated to the selected metamodeling strategy from well-established optimization procedures (Least-squares or genetic algorithms, quasi-newton methods, etc.). In this sense, the proposed strategy can be implemented in a straightforward manner by a non-expert user (i.e. a person not expert or well versed in data-driven methods).

When comparing neural networks and PCE/UK metamodels, it is interesting to evaluate the number of parameters of each model. As a preamble, it should be recalled that neural networks are a MIMO (Multiple-Input and Multiple-Output) approaches, while PCE/UK metamodels are MISO approaches. From a practical standpoint, this means that, at a particular frequency, a single model can be computed for neural networks, while $2n_s$ independent models have to be computed for PCE/UK.

For neural networks, let us consider a multilayer perceptron made of L layers. For such an architecture, the number of parameters N_{pj} at the frequency f_j is given by the following formula:

$$N_{pj} = \sum_{l=0}^L N_{l-1} \cdot N_l + \sum_{l=1}^L N_l, \quad (17)$$

where N_l is the number of nodes of the layer l . In the present study, $N_0 = M$ and $N_L = 2n_s$.

To go a little further, it is worth applying Eq. (17) to the beam and plate structures describes in sections 3 and 4, for which $(M, n_s) = (1, 2)$ and $(M, n_s) = (2, 4)$ respectively. If one considers a single hidden layer containing N_n nodes, one finds:

$$N_{pj} = \begin{cases} 6 N_n + 4 & \text{for a 1D structure (beam)} \\ 11 N_n + 8 & \text{for a 2D structure (plate)} \end{cases}. \quad (18)$$

On the contrary, for PCE/UK, the number of parameters $N_{pj}^{(i)}$ of the i^{th} metamodel ($i \in [1, 2n_s]$) at the frequency f_j is given by:

$$N_{pj}^{(i)} = \begin{cases} P & \text{for PCE} \\ P + M + 2 & \text{for UK} \end{cases}. \quad (19)$$

As an example, if $d = 3^8$, one has:

$$N_{pj}^{(i)} = \begin{cases} 4 \text{ (7)} & \text{for PCE (UK) for a 1D structure} \\ 10 \text{ (14)} & \text{for PCE (UK) for a 2D structure} \end{cases}. \quad (20)$$

The previous analysis can be summarized by saying that, compared to strategies based on neural networks, the proposed approach requires the construction of $2n_s$ times more, but less complex, metamodels. In general, a lower complexity implies a lower amount of data to fit a model (consider for instance the difference between linear and nonlinear models).

Another particularity of the proposed strategy stems from the direct use of the measured vibration signals. Except the normalization of the data to

⁸For PCE, the maximum degree of the polynomial basis is generally higher than that necessary with UK.

be independent from the excitation level, no particular feature extraction is required. In the existing literature, features extraction is generally performed and the input parameters of the metamodels are, for instance, the time of arrival of vibration waves [36, 40, 57] or the frequency integrated real and imaginary parts of the measured vibration spectra [21].

3. Numerical application

The proposed numerical application intends to assess the suitability of the strategy described above for accurately locating a point force excitation in the frequency domain. More specifically, its overall performances w.r.t. the measurement noise level in both training and deployment phases, the sensors configuration, the number of frequencies considered, as well as the optimization strategy used for solving Eq. (14) are evaluated. Consequently, this numerical application is mainly focused on the intrinsic behavior of the proposed methodology by avoiding any experimental bias, such as geometrical and material uncertainties or inaccuracies in sensors locations. In what follows, all the vibration data have been generated from a home-made code.

3.1. Problem description

The studied structure is a simply supported steel beam of length $L = 1$ m, cross-sectional area $S = 12.5 \text{ mm}^2$ and second moment of area $I = 6.5 \text{ mm}^4$, excited by a point force of amplitude F_0 between 10 Hz and 1 kHz.

In the training phase, illustrated in Fig. 4, the noiseless vibration responses $\tilde{y}_i(f_j, \mathbf{x}_k)$, corresponding to the displacement measured at frequency f_j by a set of sensors due to a unit point force applied at coordinate $x_k \in \mathcal{X}_{\text{train}}$

($M = 1$), is computed from an analytical modal expansion. Here, all the modes having a resonance frequency below 5 kHz are retained in the modal basis with a modal damping ratio set to 0.01. Then, a Gaussian white noise with a prescribed signal-to-noise ratio (SNR) is added to the noiseless data to synthesize the measured vibration response gathered in $\mathcal{Y}_{\text{train}}$.

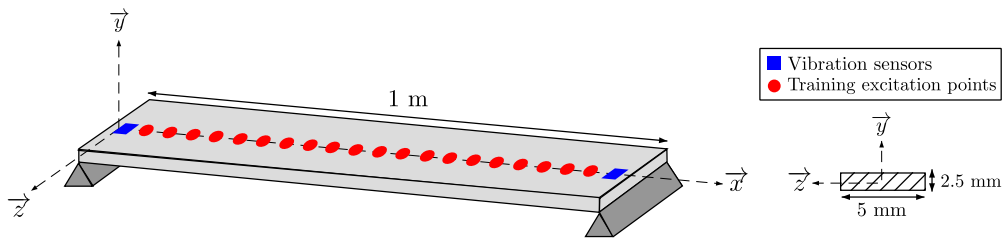


Figure 4: Illustration of the training phase

In the deployment phase, the noisy displacement data belonging to $\mathcal{Y}_{\text{test}}$ are computed from the finite element method to avoid the so-called inverse crime. The FE mesh is made up with 100 plane beam elements and the point force amplitude is set to 30 N. Similarly to the training phase, the noise corrupting the data is an additive white Gaussian noise with a prescribed SNR, assumed different from that used in the training phase. From a practical standpoint, this means that different sets of sensors and point force amplitudes are used for training and exploiting the metamodel. In doing so, the generalization ability of the present localization strategy can be evaluated.

In absence of contradictory information, the default configuration considered throughout this section is the following:

- Sensor configuration

- Number of sensors: 2 ($2n_s = 4$).
- Sensors locations⁹: 1 cm and 99 cm.
- Frequency resolution: 110 Hz ($n_f = 10$ evenly spaced frequencies).
- Training phase
 - Point force amplitude: 1 N.
 - $\mathcal{X}_{\text{train}}$: 100 evenly-spaced excitation points ($n_e = 100$).
 - \mathcal{X}_{val} : 10^4 randomly distributed excitation points ($n'_e = 10^4$).
 - SNR for $\mathcal{Y}_{\text{train}}$ and \mathcal{Y}_{val} : 25 dB.
- Deployment phase
 - Point force amplitude: 30 N.
 - $\mathcal{X}_{\text{test}}$: 10^4 randomly distributed excitation points ($n''_e = 10^4$).
 - SNR for $\mathcal{Y}_{\text{test}}$: 20 dB.
 - Spatial resolution for brute-force search: 1 mm.
 - Swarm size for PSO: 10

3.2. Application

This first application aims at illustrating the results that can be expected by applying the localization strategy for the default configuration described in the previous section. For this particular configuration, the results obtained for the three metamodeling techniques considered previously and using either the brute-force search or PSO in the localization step are presented in Fig. 5.

⁹All the coordinates are measured from the left end of the beam.

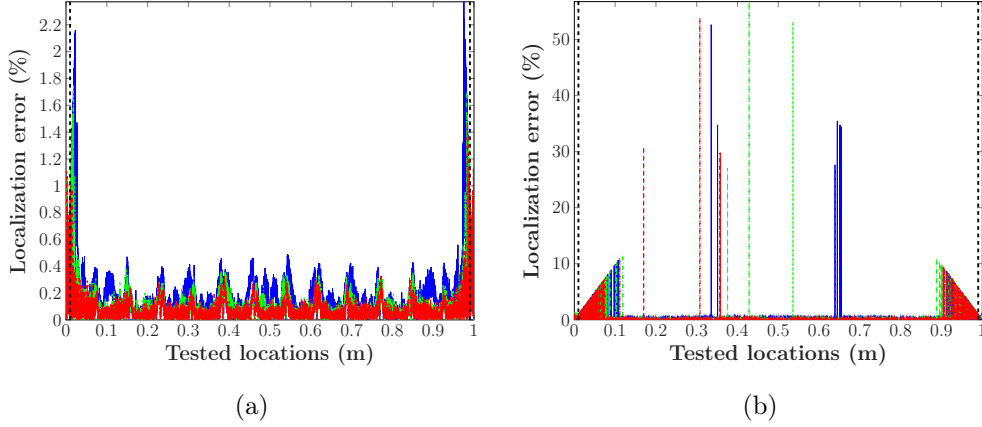


Figure 5: Spatial distribution of the localization error obtained from the default configuration from (a) Brute force search and (b) PSO for the three metamodeling techniques considered: (—) PCE, (---) QTK and (- · -) PCK – (|) Sensors locations

The qualitative analysis of these results shows that the localization performances are globally the same whatever the metamodeling method used to build the surrogate model. It is, however, interesting to note that brute-force search allows localizing a point force excitation more accurately than PSO. To confirm this observation, quantitative information are gathered in Tables 1 and 2. The localization error statistics (median and 95% CI) confirm the qualitative analysis, despite being less significant than expected. Further insights can be obtained by analyzing the value of $P_{2\%}$, corresponding to the probability of good localization within 2% (i.e. within 2 cm) in conjunction with Fig. 5b. Actually, the large discrepancies observed in Fig. 5b are rare events that are mainly concentrated close to the structure boundaries.

Table 1: Localization performances using brute-force search for three metamodeling techniques considered

	PCE	QTK	PCK
$\bar{\varepsilon}_t$ (%)	0.13	0.05	0.07
95% CI (%)	[0.006, 0.88]	[0.002, 0.27]	[0.003, 0.39]
$P_{2\%}$ (%)	99.8	100	100
T_{train} (s)	4.41	13.54	20.27
T_{test} (s)	1.15	1.15	1.17

Table 2: Localization performances using PSO search for three metamodeling techniques considered

	PCE	QTK	PCK
$\bar{\varepsilon}_t$ (%)	0.11	0.05	0.06
95% CI (%)	[0.004, 2.02]	[0.002, 1.66]	[0.003, 2.23]
$P_{2\%}$ (%)	97.4	97.8	97.3
T_{train} (s)	4.41	13.54	20.27
T_{test} (h)	12	40	88

Another interesting point is the comparison of the computation times relative to the deployment phase. Indeed, while the brute-force search requires less than 1.5 s to localize 10^4 independent point forces, PSO is far more demanding in terms of computational resources, which significantly impacts the computation times (more than half a day in the present case). To better understand the computational inefficiency of PSO, it is worth studying the shape of the objective function $J(\mathbf{x})$ to minimize in the localization step (see Eq. (14)). Fig. 6 presents the spatial distribution of $J(\mathbf{x})$, computed for the PCE, QTK and PCK metamodels, for two particular tested point force locations. It should be noticed that the objective function is highly non-convex whatever the metamodeling strategy implemented. This observation may explain the difficulty of PSO in converging rapidly to an optimal global solution. As a workaround, hybrid strategies combining global and local optimizations can be implemented, but their application is outside the scope of this paper [58]. In light of this comparison, only the brute-force search will be used in the rest of the paper.

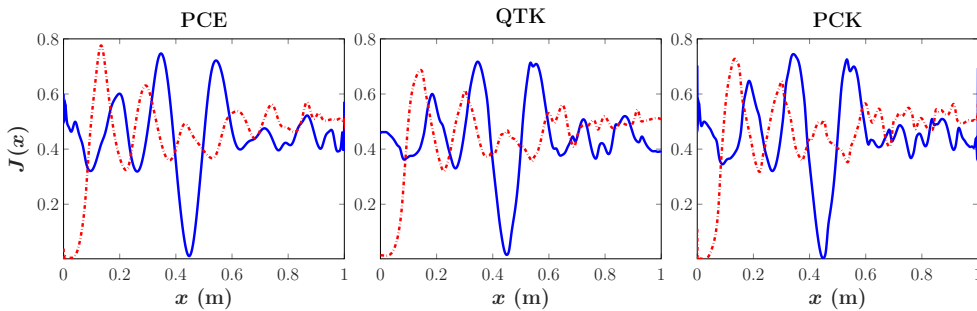


Figure 6: Objective function $J(\mathbf{x})$ associated to the PCE, QTK and PCK metamodels for two particular tested point force locations – (—) $x = 45$ cm and (· · ·) $x = 2$ cm

3.3. Influence of the measurement noise

The results presented in the previous section suggest a certain robustness of the proposed localization strategy w.r.t. to noise. To investigate this question into more details, we propose to study the influence of the measurement noise, modelled as an additive white Gaussian noise with a prescribed SNR, in both training and deployment phases on the localization performances. However, to discriminate the influence of the noise level in each phase on the localization accuracy, the procedure is applied by varying the SNR from 35 dB to 20 dB in one phase, while keeping it constant and equal to 20 dB in the other phase.

Fig. 7 (resp. Fig. 8) presents the statistics of the localization error ε_t as well as the probability of good localization $P_{2\%}$ for a varying measurement noise level in the training (resp. testing) dataset and a fixed measurement noise level in the testing (resp. training) dataset. Obtained results show that the localization accuracy is quite insensitive to the noise in the data whatever the phase considered. This conclusion can be quite counterintuitive, but is actually in line with some observations made in the field of machine learning [39, 59]. In the present case, a possible explanation could be related to the use of polynomial bases to build the various metamodels that tends to "regularize" the surrogate model. Practically, this observation results in a value of the global predictivity Q_2^g coefficient between 72% and 92% for the considered measurement noise levels.

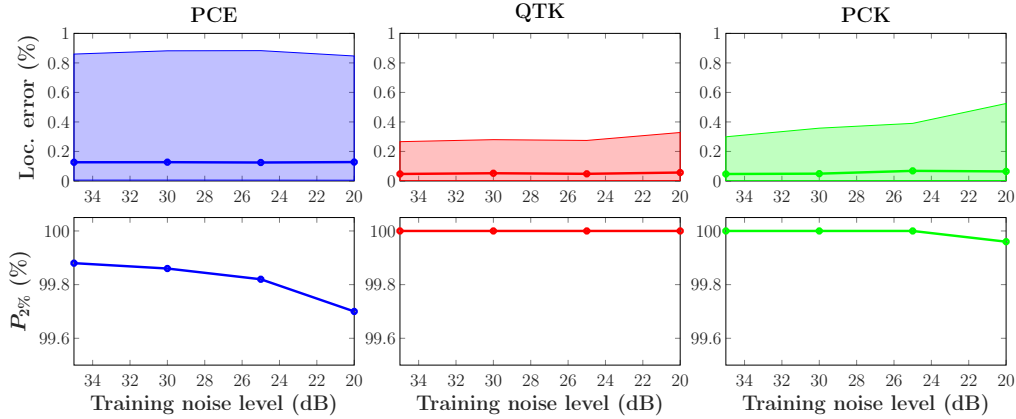


Figure 7: Influence of the measurement noise level in $\mathcal{Y}_{\text{train}}$ on the localization performances for the PCE, QTK and PCK metamodels and 20 dB SNR in $\mathcal{Y}_{\text{test}}$ – (first row) Statistics of the localization error: median $\bar{\varepsilon}_t$ and 95% CI, (second row) $P_{2\%}$: Probability of good localization within 2%

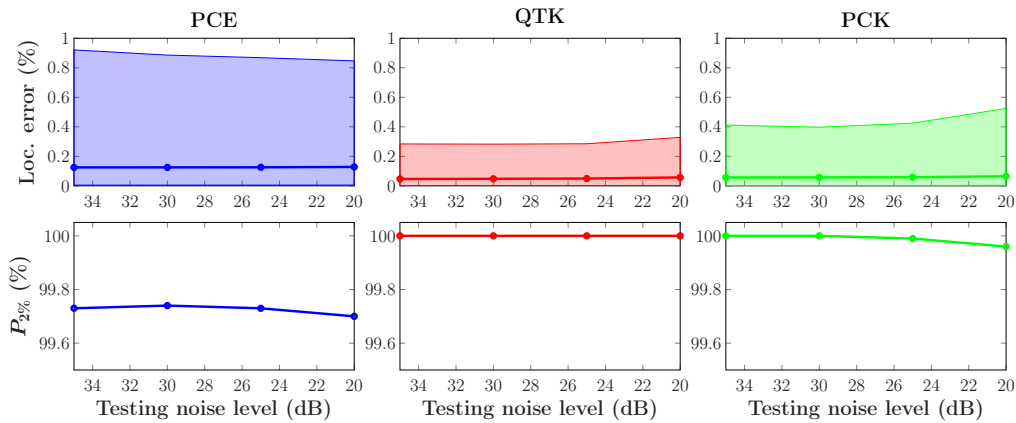


Figure 8: Influence of the measurement noise level in $\mathcal{Y}_{\text{test}}$ on the localization performances for the PCE, QTK and PCK metamodels and 20 dB SNR in $\mathcal{Y}_{\text{train}}$ – (first row) Statistics of the localization error: median $\bar{\varepsilon}_t$ and 95% CI, (second row) $P_{2\%}$: Probability of good localization within 2%

3.4. Influence of the number of frequencies considered

Until now, 10 evenly spaced frequencies (from 10 Hz to 1 kHz) have been used to apply the proposed localization strategy. In particular, this demonstrates that considering all the frequency content of the collected data is not necessary to obtain accurate solutions. An interesting side effect is that a trade-off between the computational efficiency and the localization accuracy can be obtained by restricting the useful information to only a particular subset of the measured vibration data. In this regard, it could be interesting to determine the minimal number of frequencies required to obtain satisfying localization performances. To this end, we propose to apply the proposed localization strategy for six frequency sets, noted F_i in the following, where i is the number of frequencies included in a particular set. The frequency sets considered in this section are defined in Table 3. It should be noted here that the frequencies included in each set F_i are not resonance frequencies. Indeed, at these specific frequencies, the dynamic response of lightly damped structures is mainly driven by its vibration modes implying that these frequencies don't convey any useful information on the point force location.

Fig. 9 presents the results obtained for the six frequency sets F_i . The immediate conclusion is that using only one frequency is not sufficient to obtain satisfying localization performances, since $P_{2\%}$ is about 40%, while the median localization error is about 20% for PCE, QTK and PCK metamodels. This result can be potentially problematic for harmonic excitations. In this situation, the number of sensors used to measure the vibration data needs to be increased (see section 3.5). From two frequencies, the localization are

Table 3: Definition of six frequency sets F_i

Set ID	Frequencies (Hz)
F_1	500
F_2	{330, 660}
F_3	{250, 500, 750}
F_5	{125, 250, 500, 750, 825}
F_{10}	Range = [10, 1000], Resolution = 110
F_{20}	Range = [10, 1000], Resolution = 52.1

drastically improved, since the median localization errors is less than 0.2%, while $P_{2\%}$ is greater than 99.7% (see Fig. 10).

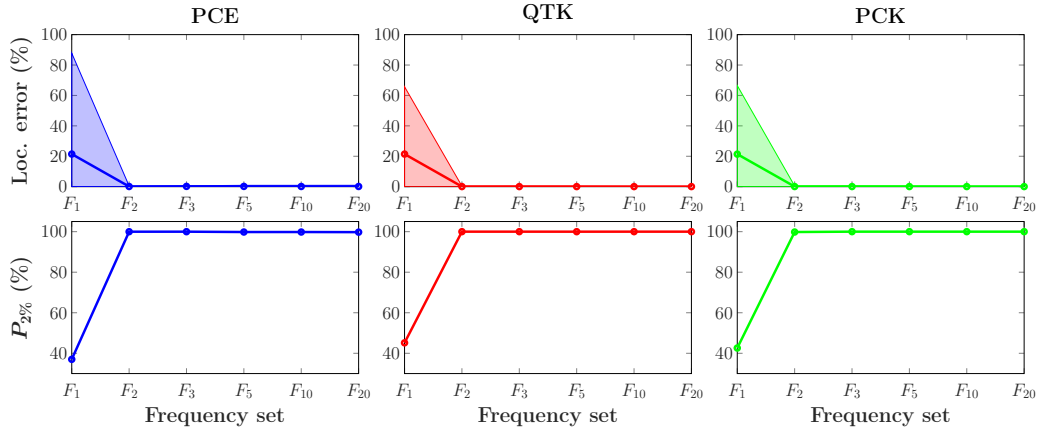


Figure 9: Influence of the number of frequencies considered in the localization procedure – (first row) Statistics of the localization error: median $\bar{\varepsilon}_t$ and 95% CI, (second row) $P_{2\%}$: Probability of good localization within 2%

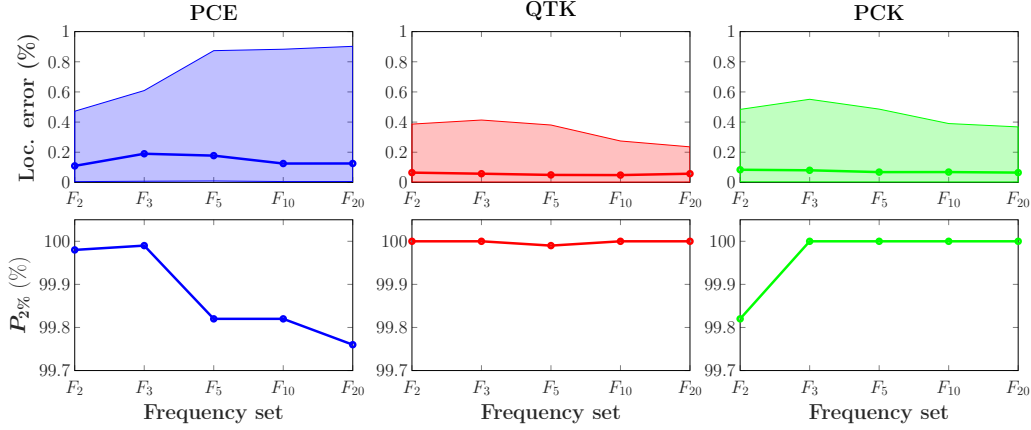


Figure 10: Influence of the number of frequencies considered in the localization procedure: Restriction to $[F_2, F_{20}]$ – (first row) Statistics of the localization error: median $\bar{\varepsilon}_t$ and 95% CI, (second row) $P_{2\%}$: Probability of good localization within 2%

3.5. Influence of the number of sensors

It has been shown in section 3.4 that using only one frequency and two sensors does not lead to satisfying localization performances. This observation is somewhat problematic for harmonic excitation. The solution to improve the localization accuracy consists in increasing the number of sensors used to collect the training and testing data. Fig. 11 presents the evolution of the statistics of the localization error, as well as that of the probability of good reconstruction within 2% w.r.t. the number of sensors (evenly distributed over the structure). This figure shows that from 5 sensors the amount of information is sufficient to properly locate 73% of the point forces from the PCE metamodel, while this value reaches 91% for the QTK and PCK metamodels. In this case, however, the 95% CIs remain relatively large, even if the median localization errors are below 1%. Here, to significantly reduce the width of the CI and consequently improve the probability

of good localization, at least 10 sensors, evenly distributed over structure, are necessary (see Fig. 12).

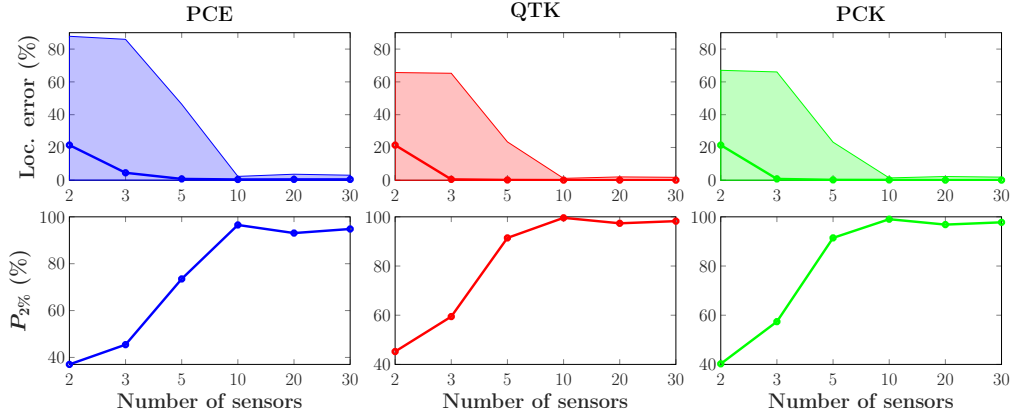


Figure 11: Influence of the number of sensors for the frequency set F_1 – (first row) Statistics of the localization error: median $\bar{\varepsilon}_t$ and 95% CI, (second row) $P_{2\%}$: Probability of good localization within 2%

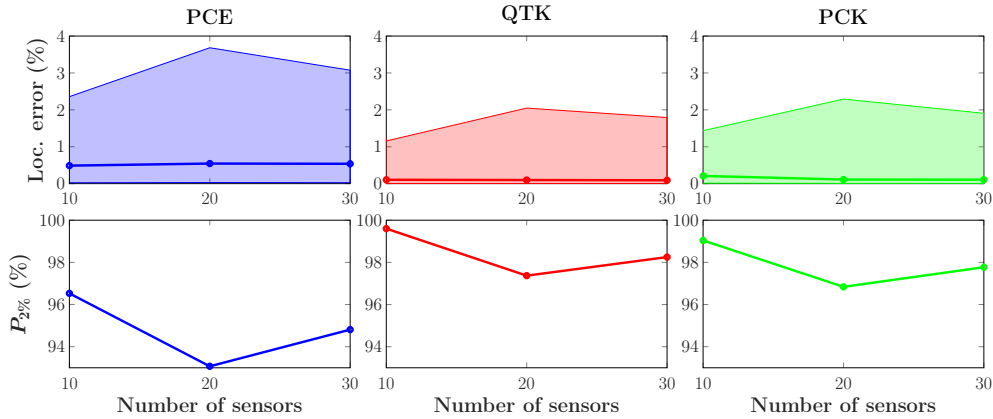


Figure 12: Influence of the number of sensors for the frequency set F_1 : Restriction to the interval $[10, 30]$ – (first row) Statistics of the localization error: median $\bar{\varepsilon}_t$ and 95% CI, (second row) $P_{2\%}$: Probability of good localization within 2%

3.6. Influence of the size of the training set

As any metamodel-based technique, the accuracy of the proposed localization strategy is mainly conditioned to the quality of the surrogate model built from the information collected in the training set $\mathcal{T}_{\text{train}}$. In this section, we are more precisely interested in the influence of the number of training point force locations on the localization performances. To this end, the localization procedure is applied by varying the number of training point force locations from 10 to 100, corresponding to a spatial resolution comprised between 10 cm and 1 cm. As shown in Fig. 13, a too low number of training point force location leads to poor localization performances. This can be actually related to the value of the predictivity coefficient, which is below 7% for the PCE, QTK and PCK metamodels when considering 10 training point force locations. From 20 point force locations, the metamodels are predictive and the localization performances are improved accordingly (see Fig. 14).

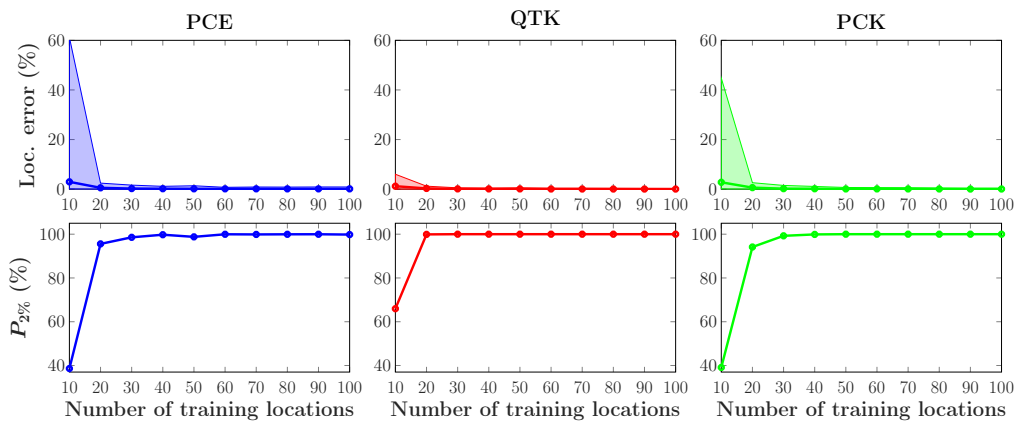


Figure 13: Influence of the size of the training set – (first row) Statistics of the localization error: median $\bar{\varepsilon}_t$ and 95% CI, (second row) $P_{2\%}$: Probability of good localization within 2%

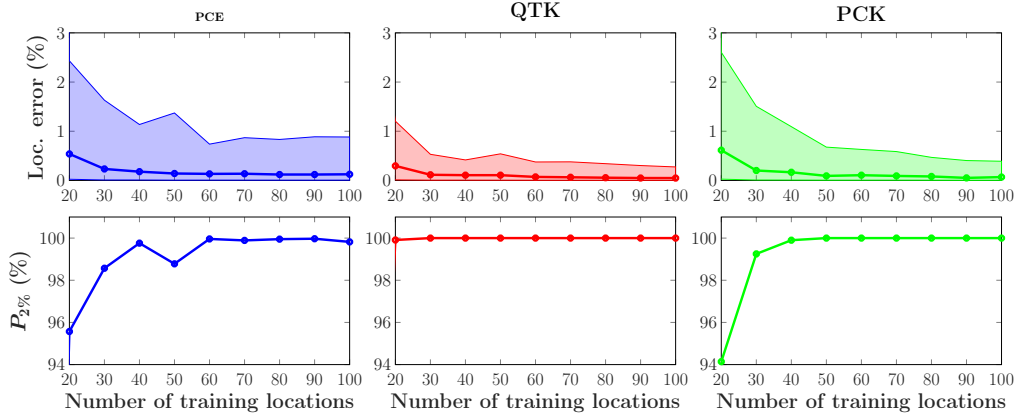


Figure 14: Influence of the size of the training set: Restriction to the interval $[20, 100]$ – (first row) Statistics of the localization error: median $\bar{\varepsilon}_t$ and 95% CI, (second row) $P_{2\%}$: Probability of good localization within 2%

3.7. Influence of the sensor configuration

When implementing a data-driven strategy, one of the crucial issue concerns the type, the number and the location of the sensors used to record the data. In the present case, using displacement, velocity or acceleration data has almost no influence, since the methodology is applied in the frequency domain. On the contrary, the location and the number of sensors may have a significant impact on localization performances. To better assess the influence of the sensor configuration, let us consider two particular configurations: (i) one sensor located at 1 cm from the left end of the beam and two sensors located at 30 cm and 70 cm from the left end of the beam. For these configurations, the spatial distributions of the localization error, obtained from the PCE, QTK and PCK metamodels, are presented in Fig. 15. This figure highlights an interesting phenomenon, since an abrupt increase in the localization error is observed closed to the boundaries of the beam. A

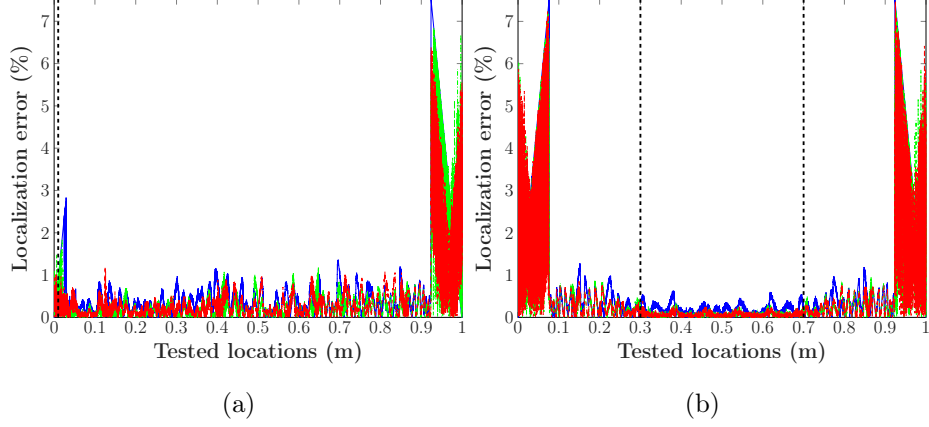


Figure 15: Spatial distribution of the localization error obtained for a sensor configuration using (a) one sensor located at 1 cm and (b) two sensors located at 30 cm and 70 cm from the left end of the beam and considering 10 frequencies in [10 Hz, 1 kHz]: (—) PCE, (---) QTK and (- · -) PCK - (|) Sensors locations

careful analysis shows that the length of this region is equal to half of the bending wavelength computed at the maximal frequency considered, 1 kHz in the present case. At this particular frequency, the half bending wavelength is equal to 7.6 cm. Consequently, larger localization errors are expected in the regions [0 cm, 7.6 cm] and [92 cm, 100 cm] if no sensor is placed in these sections, which is actually observed in Figs. 15a and 15b.

To confirm this observation, the localization procedure is now applied by extending the frequency range up to 2 kHz, while keeping the same frequency resolution. In this case, the half bending wavelength is equal to 5.4 cm. Consequently, large localization errors are expected in the regions [94 cm, 100 cm] and/or [0, 5.4 cm], as confirmed in Fig. 16. It is also worth mentioning that increasing the frequency range allows not only reducing the size of the

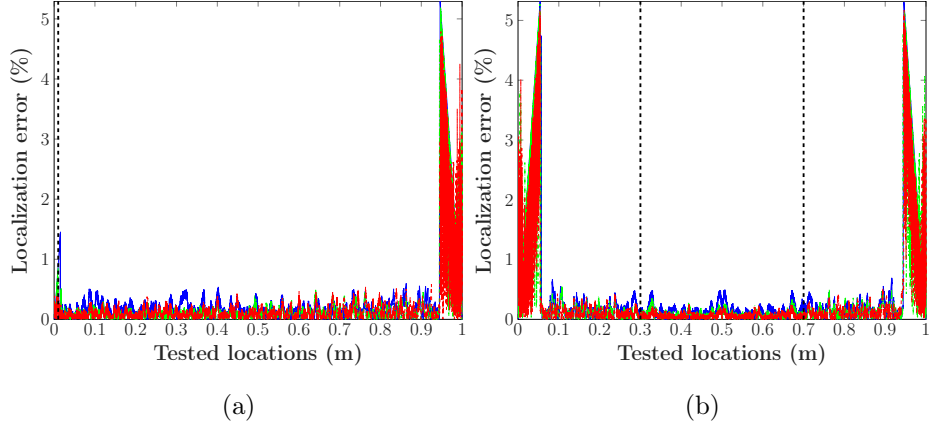


Figure 16: Spatial distribution of the localization error obtained for a sensor configuration using (a) one sensor located at 1 cm and (b) two sensors located at 30 cm and 70 cm from the left end of the beam and considering 20 frequencies in [10 Hz, 2 kHz]: (—) PCE, (---) QTK and (- · -) PCK - (|) Sensors locations

region of large localization error but also decreasing the value of the maximal localization error. Indeed, in the present situation, the maximal localization error goes from 7.5% to 5.3% (see Figs. 15 and 16). As a side note, one can notice that even with a single sensor, it is possible to accurately localize point force excitations (see Table 4).

3.8. Summary

This numerical application intended to answer the main practical issues that can arise when implementing the proposed purely data-driven localization procedure. In summary, the following conclusions can be drawn:

- The proposed procedure is robust to noise in the data in both training and deployment phases.

Table 4: Localization performances for a single sensor depending on the maximal frequency f_{\max}

		PCE	QTK	PCK
$f_{\max} = 1$ kHz	$\bar{\varepsilon}_t$ (%)	0.33	0.21	0.17
	95% CI (%)	[0.02, 5.13]	[0.009, 2.63]	[0.007, 3.22]
	$P_{2\%}$ (%)	93.8	96.4	95.7
$f_{\max} = 2$ kHz	$\bar{\varepsilon}_t$ (%)	0.15	0.09	0.08
	95% CI (%)	[0.008, 2.62]	[0.004, 1.57]	[0.003, 1.81]
	$P_{2\%}$ (%)	96.7	98.2	97.7

- There exists two practical ways of improving the localization accuracy. They mainly consists in increasing the number of vibration sensors and/or the frequency range.
- The number of training point force locations must be sufficient to ensure a fairly good representativeness of the metamodel. Following our observations, the training dataset should be chosen so as to obtain a predictivity coefficient between 70% and 90%. In doing so, the metamodel built from the training dataset is expected to generalize pretty well.
- If point forces are expected to act in the vicinity of the boundaries of the studied structure, it is recommended either to place a sensor at most at the half wavelength from the structure boundary or to increase the frequency range considered in the analysis.
- Accurate localizations can be obtained with a single sensor.

- QTK performs generally better than PCE and PCK.

4. Real-world application

In this section, a real-world application is carried out on a real-world application in order to confirm some of the conclusions drawn in the previous numerical experiment.

4.1. Description of the experimental set-up

The structure under test is a thin aluminum plate of 60 cm in length, 40 cm in width and 6 mm in thickness, clamped along its length in a wooden support. The effective width of the plate resulting from the mounting conditions is 39.1 cm. To perform all the subsequent measurements the system is suspended to a rigid structure through a set of elastic bungee cords (see Fig. 17).

To form the training set \mathcal{T} , the validation set \mathcal{V} and the test set \mathcal{S} , a collection of Frequency Response Functions (FRF) is estimated using a roving hammer procedure for four accelerometers ($n_s = 4$) located at the corners of a grid of 17×17 excitation points (see Fig. 17). Practically, the impact hammer has been equipped with a steel tip in order to properly excite the structure until 6.5 kHz. For the sake of the completeness, it must be said that each FRF has been estimated from the vibration responses resulting from three consecutive impacts. Consequently, considering a frequency resolution of 0.5 Hz, the experimental dataset \mathcal{E} is the collection of an input dataset \mathcal{X}_{exp} of 289×2 elements ($M = 2$), corresponding to the coordinates $(x_{\text{exp}}, y_{\text{exp}})$ of the 289 point forces, and an output dataset \mathcal{Y}_{exp} of $289 \times 8 \times 13000$ elements,



Figure 17: Structure under test – Definition of the grid of excitation points

corresponding to all the estimated FRFs, normalized using the procedure described in section 2.2.2.

It results from what precedes that the training and validation sets, \mathcal{T} and \mathcal{V} , are actually defined as a particular subset of \mathcal{E} . The test set \mathcal{S} is built from the FRFs measured for the point force locations contained in \mathcal{X}_{val} ¹⁰. More specifically, each FRF is multiplied by the average force spectrum estimated from the three consecutive impacts at the corresponding excitation location in order to obtain a set of acceleration responses. Finally, these vibration responses are normalized to form the output dataset $\mathcal{Y}_{\text{test}}$.

¹⁰Using \mathcal{X}_{val} in both validation and test steps does not bias the results, since here the validation dataset only serves to assess the metamodel quality and not to improve it.

In absence of contradictory information, the default configuration considered in this experimental application is presented in Fig. 18. In this configuration, odd numbered excitation points define the input dataset $\mathcal{X}_{\text{train}}$, while even numbered excitation points form the validation (resp. test) dataset \mathcal{X}_{val} (resp. $\mathcal{X}_{\text{test}}$). The output datasets $\mathcal{Y}_{\text{train}}$, \mathcal{Y}_{val} and $\mathcal{Y}_{\text{test}}$ are derived from \mathcal{Y}_{exp} by restricting the dataset to 20 evenly spaced frequencies between 100 Hz and 2 kHz (frequency resolution: 100 Hz). This implies that $\mathcal{Y}_{\text{train}}$ has $145 \times 8 \times 20$ elements, while \mathcal{Y}_{val} and $\mathcal{Y}_{\text{test}}$ have $144 \times 8 \times 20$ elements.

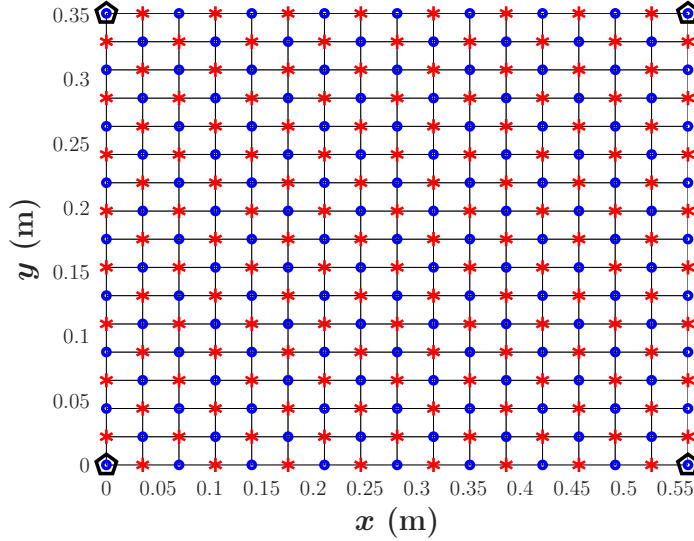


Figure 18: Default configuration – (\circ) $\mathcal{X}_{\text{train}}$, ($*$) $\mathcal{X}_{\text{val}} = \mathcal{X}_{\text{test}}$ and (\diamond) Acceleration sensors

4.2. Application

The application of the proposed localization procedure to the default configuration leads to the results summarized in Table 5 and presenting the localization error statistics (median and 95% CI) as well as the probability of

locating a point force within 3% (i.e. within a circle of radius 2 cm). As for the numerical application, accurate localizations are obtained, proving that the proposed method is also applicable to real mechanical structures.

Table 5: Localization performances for the default configuration

	PCE	QTK	PCK
$\bar{\varepsilon}_t$ (%)	1.22	0.76	1.08
95% CI (%)	[0.15, 3.05]	[0.14, 2.07]	[0.24, 3.10]
$P_{3\%}$ (%)	95.8	99.3	96.5
T_{train} (s)	86.4	97.5	231.3
T_{test} (s)	19.1	21.3	18.1

Results have been obtained using a brute-force search approach in the localization phase. Of course, more sophisticated optimization strategies can be implemented, but their performance would be strongly affected by the shape of the objective function to minimize. In the present case, the objective function is highly non-convex (see Fig. 19), implying that the optimization algorithm has to be chosen and applied with care.

4.3. Influence of the maximal frequency considered

As suggested in section 3.7, the frequency range retained to perform the analysis can have a beneficial impact on the localization accuracy. To confirm this observation, the localization procedure is applied by ranging the maximal frequency considered from 1 kHz to 5 kHz, while keeping the frequency resolution constant to 100 Hz. The results presented in Fig. 20 indeed reveal

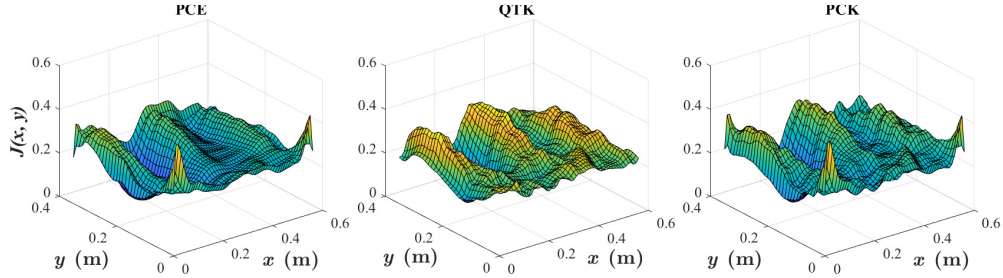


Figure 19: Objective function $J(x, y)$ associated to the PCE, QTK and PCK metamodells for an actual point force located at point $(x, y) = (17.6 \text{ cm}, 26.4 \text{ cm})$ of the experimental grid

an effect of the maximal frequency retained for the analysis, since the median localization error tends to decrease whatever the metamodelling strategy implemented. Regarding the width of the CI, it is interesting to note that it continuously decreases for the QTK metamodell, while it remains almost constant from a maximal frequency of 2 kHz for the PCE and PCK metamodells. This behavior has a direct impact on $P_{3\%}$, the probability of good reconstruction within 3%, which tends to stabilize from 2 kHz¹¹.

4.4. Influence of the training configuration

In this section, the influence of the training configuration is studied. To this end, four configurations are considered and presented in Fig. 21. More precisely, the input datasets $\mathcal{X}_{\text{train}}$, \mathcal{X}_{val} and $\mathcal{X}_{\text{test}}$ are derived from the experimental input dataset \mathcal{X}_{exp} and satisfy the relations:

$$\mathcal{X}_{\text{exp}} = \mathcal{X}_{\text{train}} \cup \mathcal{X}_{\text{val}} \text{ and } \mathcal{X}_{\text{exp}} = \mathcal{X}_{\text{train}} \cup \mathcal{X}_{\text{test}}. \quad (21)$$

¹¹Given the number of excitation points in $\mathcal{X}_{\text{test}}$, namely 144, an increase in $P_{3\%}$ by 1.4% corresponds to two additional locations properly estimated.

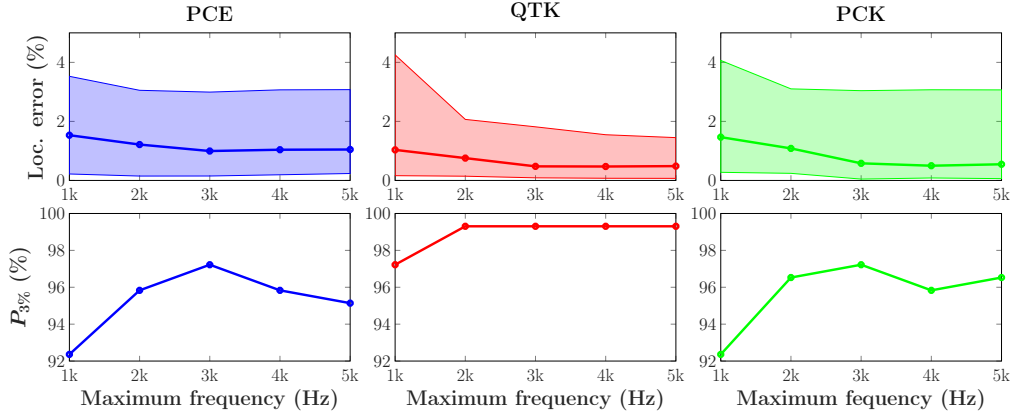
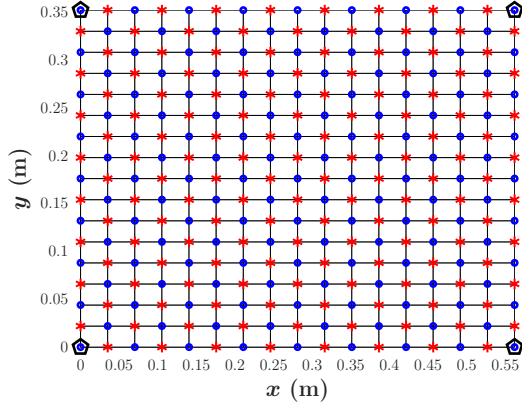


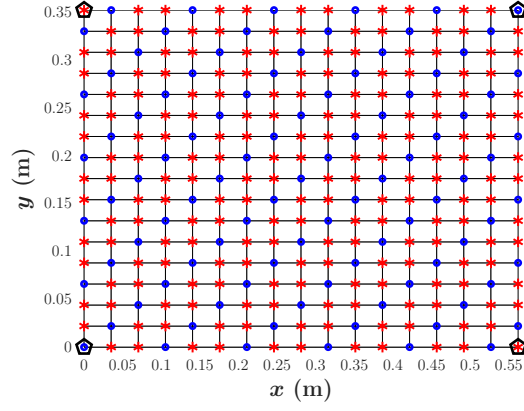
Figure 20: Influence of the maximal frequency retained in the analysis – (first row) Statistics of the localization error: median $\bar{\varepsilon}_t$ and 95% CI, (second row) $P_{3\%}$: Probability of good localization within 3%

Here, configuration C_1 corresponds to the default configuration presented in Fig. 18 and recalled in Fig. 21a for the sake of comparison. In configuration C_2 , 1 point out of 3, i.e. 97 in total, is retained to form $\mathcal{X}_{\text{train}}$ (see Fig. 21b), while 1 point out of 4, i.e. 73 in total, is kept in configuration C_3 to build the input training dataset (see Fig. 21c). Finally, configuration C_4 defines $\mathcal{X}_{\text{train}}$ as a collection of 100 randomly chosen excitation points (see Fig. 21d).

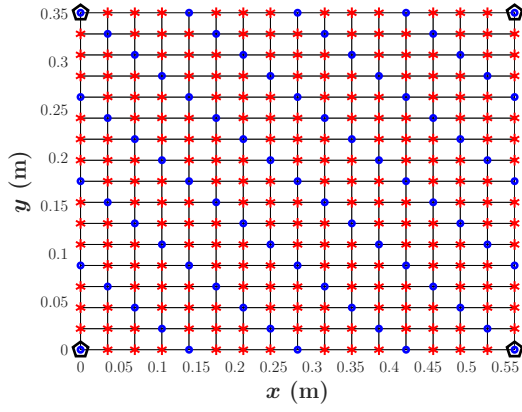
Fig. 22 summarizes the results obtained for the four configurations described above. The analysis of the results calls for two conclusions. First, the denser the spatial distribution of training excitation points is, the better the localization accuracy is. Second, we observe that training the meta-models from data collected on a regular grid allows obtaining more accurate localizations than those resulting from a random-grid-based training.



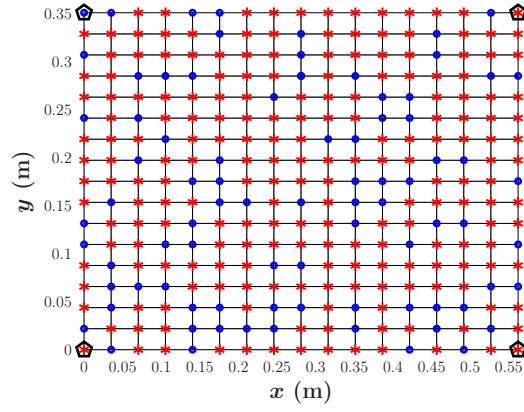
(a)



(b)



(c)



(d)

Figure 21: Definition of the studied configuration – (a) Configuration C_1 : default, (b) Configuration C_2 , (c) Configuration C_3 and (d) Configuration C_4 – (\circ) $\mathcal{X}_{\text{train}}$, ($*$) $\mathcal{X}_{\text{val}} = \mathcal{X}_{\text{test}}$ and (\diamond) Acceleration sensors

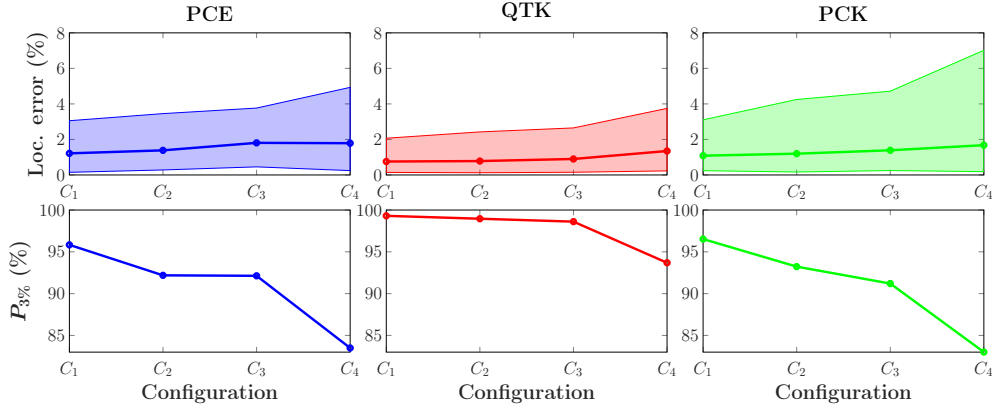


Figure 22: Influence of the size of the training set – (first row) Statistics of the localization error: median $\bar{\varepsilon}_t$ and 95% CI, (second row) $P_{3\%}$: Probability of good localization within 3%

4.5. Applicability for one vibration sensor

The results presented in section 3.7 have shown that using a single vibration sensor could lead to reasonable localization performances. This property is interesting in a practical context where having a large number of sensor is not always possible. In this section, it is intended to assess the localization accuracy of the proposed approach by using the information provided by each of the four acceleration sensors mounted on the structure. The ID and the coordinates of each sensor, measured from the point (0, 0) of the excitation grid (see Fig. 18), are defined in Table 6.

Fig. 23 shows that the localization performances are better when the sensor is located close to clamped edge (A_1 and A_2). A closer analysis of the results indicates that all the point force locations are estimated within a circle of radius 3.3 cm for A_1 and A_2 , 5.7 cm for A_3 and 4.6 cm for A_4 .

Table 6: Definition of the ID and the coordinates of each acceleration sensor

ID	Coordinates (x, y) (cm)
A_1	(0, 0)
A_2	(56.2, 0)
A_3	(0, 35.1)
A_4	(56.2, 35.1)

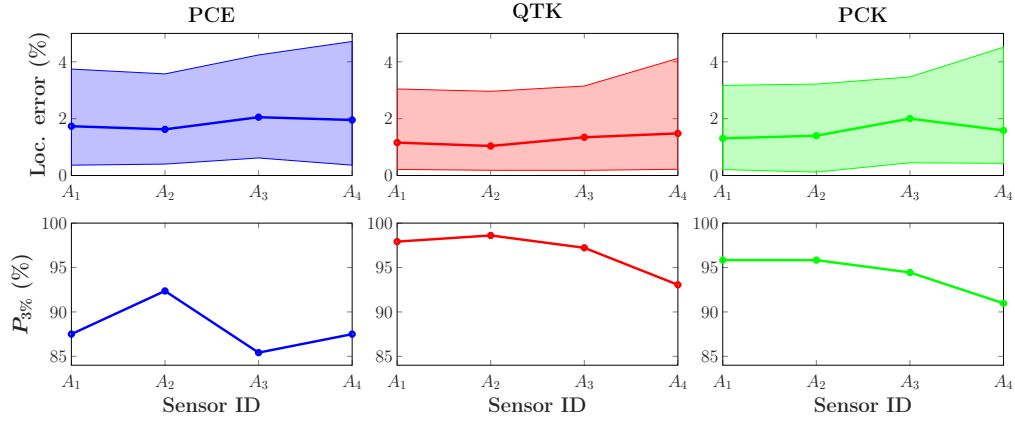


Figure 23: Applicability for one acceleration sensor – (first row) Statistics of the localization error: median $\bar{\varepsilon}_t$ and 95% CI, (second row) $P_{3\%}$: Probability of good localization within 3%

4.6. Summary

The results presented in this experimental validation allows confirming some of the conclusions drawn from the numerical validation conducted in section 3. More specifically, it has been shown in this section that:

- The maximal frequency considered in the analysis has a direct influence on the localization accuracy.
- Training the metamodels from data collected on a regular grid allows obtaining more accurate localizations than those resulting from a random-grid-based training.
- A single vibration sensor can be used for point force localization. However, the larger the number of sensors is, the better the localization performances are.
- QTK performs globally better than PCE and PCK.

5. Conclusion

This paper has introduced a novel data-driven approach, based on the used of classical metamodeling strategies, for localizing point force excitations in the frequency domain. The proposed localization method is divided into a training stage, in which a metamodel is built, and a deployment phase, consisting in an optimization procedure taking advantage of the metamodel to efficiently estimate the point force location given new vibration data. In the course of this paper, three metamodeling techniques have been tested: Polynomial Chaos Expansion (PCE), Quadratic Trend Kriging (QTK) and

Polynomial Chaos Kriging (PCK). From the numerical and experimental validations conducted, it has been demonstrated that the proposed approach is robust to noise and allows accurate localizations for relatively small datasets and sparse sensors configurations. In addition, we have shown that QTK metamodel leads to localizations more accurate than those obtained from PCE and PCK metamodels. Finally, a single vibration sensor can potentially be used provided the structure is rather simple and/or the localization region has limited extent.

References

- [1] C. Renzi, C. Pezerat, and J.-L. Guyader. Vibratory source identification by using the Finite Element Model of a subdomain of a flexural beam. *Journal of Sound and Vibration*, 332:545–562, 2013.
- [2] A. Rezaayat, V. Nassiri, B. De Pauw, J. Ertveldt, S. Vanlanduit, and P. Guillaume. Identification of dynamic forces using group-sparsity in frequency domain. *Mechanical Systems and Signal Processing*, 70-71:756–768, 2016.
- [3] M. Aucejo and O. De Smet. A multiplicative regularization for force reconstruction. *Mechanical Systems and Signal Processing*, 85:730–745, 2017.
- [4] C. Faure, F. Ablitzer, J. Antoni, and C. Pezerat. Empirical and fully Bayesian approaches for the identification of vibration sources from transverse displacement measurements. *Mechanical Systems and Signal Processing*, 94:180–201, 2017.

- [5] M. Aucejo, O. De Smet, and J.-F. Deü. Practical issues on the applicability of Kalman filtering for reconstructing mechanical sources in structural dynamics. *Journal of Sound of Vibration*, 442:45–70, 2019.
- [6] W. Feng, Q. Li, and Q. Lu. Force localization and reconstruction based on a novel sparse Kalman filter. *Mechanical Systems and Signal Processing*, 144:106890, 2020.
- [7] C. Pezerat and J.-L. Guyader. Two inverse methods for localization of external sources exciting a beam. *Acta Acustica*, 3:1–10, 1995.
- [8] Q. Leclere and C. Pezerat. Vibration source identification using corrected finite difference schemes. *Journal of Sound and Vibration*, 331:1366–1377, 2012.
- [9] N. Aujogue and A. Ross. Transient force analysis technique to identify time-varying loads and defects of plates. In *Proceedings of the 26th International Congress on Sound and Vibration (ICSV 26)*, Montreal, Canada, July 2019.
- [10] A. Berry, O. Robin, and F. Pierron. Identification of dynamic loading on a bending plate using the Virtual Fields Method. *Journal of Sound and Vibration*, 333:7151–7164, 2014.
- [11] P. O’Donoghue, O. Robin, and A. Berry. Time-resolved identification of mechanical loadings on plates using the virtual fields method and deflectometry measurements. *Strain*, 54 (3):e12258, 2018.

- [12] Q. Li and Q. Lu. Impact localization and identification under a constrained optimization scheme. *Journal of Sound and Vibration*, 366:133–148, 2016.
- [13] G. Yan, H. Sun, and O. Büyüköztürk. Impact load identification for composite structures using Bayesian regularization and unscented Kalman filter. *Structural Control and Health Monitoring*, 24 (5):e1910, 2017.
- [14] B.-T. Wang and C.-H. Chiu. Determination of unknown impact force acting on a simply supported beam. *Mechanical Systems and Signal Processing*, 17 (3):683–704, 2003.
- [15] P. Logan, P. Avitabile, and J. Dodson. Reconstruction of external forces beyond measured points using a modal filtering decomposition approach. *Experimental techniques*, 44:113–125, 2020.
- [16] D. Goutaudier, D. Gendre, V. Kehr-Candille, and R. Ohayon. Single-sensor approach for impact localization and force reconstruction by using discriminating vibration modes. *Mechanical Systems and Signal Processing*, 138:106534, 2020.
- [17] E. Jacquelin, A. Bennani, and P. Hamelin. Force reconstruction: analysis and regularization of a deconvolution problem. *Journal of Sound and Vibration*, 265:81–107, 2003.
- [18] B. Qiao, X. Zhang, J. Gao, R. Liu, and X. Chen. Sparse deconvolution for the large-scale ill-posed inverse problem of impact force reconstruction. *Mechanical Systems and Signal Processing*, 83:93–115, 2017.

- [19] E. Lourens, C. Papadimitriou, S. Gillijns, E. Reynders, G. De Roeck, and G. Lombaert. Joint input-response estimation for structural systems based on reduced-order models and vibration data from a limited number of sensors. *Mechanical Systems and Signal Processing*, 29:310–327, 2012.
- [20] O. Sedehi, C. Papadimitriou, D. Teymouri, and L. S. Katafygiotis. Sequential Bayesian estimation of state and input in dynamical systems using output-only measurements. *Mechanical Systems and Signal Processing*, 131:659–688, 2019.
- [21] R. T. Jones, J. S. Sirkis, and E. J. Friebele. Detection of impact location and magnitude for isotropic plates using neural networks. *Journal of Intelligent Material Systems and Structures*, 7:90–99, 1997.
- [22] Y. Zhong, J. Xiang, H. Gao, and Y. Zhou. Impact energy level assessment of composite structures using MUSIC-ANN approach. *Structural Control and Health Monitoring*, 23:825–837, 2016.
- [23] I. Tabian, H. Fu, and Z. S. Khodaei. A convolutional neural network for impact detection and characterization of complex composite structures. *Sensors*, 19 (22):4933, 2019.
- [24] J. M. Zhou, L. Dong, W. Guan, and J. Yan. Impact load identification of nonlinear structures using deep Recurrent Neural Network. *Mechanical Systems and Signal Processing*, 133:106292, 2019.
- [25] J. Park, S. Ha, and F.-K. Chang. Monitoring impacts events using a system-identification method. *AIAA Journal*, 47 (9):2011–2021, 2009.

- [26] W. J. Staszewski, S. Mahzan, and R. Traynor. Health monitoring of aerospace composite structures - Active and passive approach. *Composites Science and Technology*, 69 (11-12):1678–1685, 2009.
- [27] S. Ahmari and M. Yang. Impact location and load identification through inverse analysis with bounded uncertain measurements. *Smart Materials and Structures*, 22:085024, 2013.
- [28] G. Zhao, H. Hu, S. Li, L. Liu, and K. Li. Localization of impact on composite plates based on integrated wavelet transform and hybrid minimization algorithm. *Composite Structures*, 176:234–243, 2017.
- [29] S. Atobe, S. Nonami, N. Hu, and H. Fukunaga. Identification of impact force acting on composite laminated plates using the radiated sound measured with microphones. *Journal of Sound and Vibration*, 405:251–268, 2017.
- [30] E. Bavu, A. Berry, V. Gibiat, and C. Besnainou. Super-resolution imaging of active sound and vibrational sources using a time-reversal sink. In *Proceedings of Acoustics'08*, Paris, France, June 2008.
- [31] J. Frieden, J. Cugnoni, J. Botsis, and T. Gmür. Low energy impact damage monitoring of composites using dynamic strain signals from FBG sensors - Part I: Impact detection and localization. *Composite Structures*, 94:438–445, 2012.
- [32] M. Ruiz, L. E. Mujica, X. Berjaga, and J. Rodellar. Partial least square/projection to latent structures (PLS) regression to estimate

- impact localization in structures. *Smart Materials and Structures*, 22:025028, 2013.
- [33] Q. Xu. A comparison study of extreme learning machine and least squares support vector machine for structural impact localization. *Mathematical Problems in Engineering*, 2014:906732, 2014.
- [34] N. Sanchez, V. Meruane, and A. Oritz-Bernardin. A novel impact identification algorithm based on a linear approximation with maximum entropy. *Smart Materials and Structures*, 25:095050, 2016.
- [35] H. T. Hahn, B. Wilkerson, and J. Stuart. An artificial neural network for low-energy impact monitoring. *Journal of Thermoplastic Composite Materials*, 7 (4):344–351, 1994.
- [36] K. Worden and W. J. Staszewski. Impact location and quantification on a composite panel using neural networks and a genetic algorithm. *Strain*, 36 (2):61–68, 2000.
- [37] D.-U. Sung, J.-H. Oh, C.-G. Kim, and C.-S. Hong. Impact monitoring of smart composite laminates using neural network and wavelet analysis. *Journal of Intelligent Material Systems and Structures*, 11 (3):180–190, 2000.
- [38] S. Mahzan, W. J. Staszewski, and K. Worden. Experimental studies on impact damage location in composite aerospace structures using genetic algorithms and neural networks. *Smart Structures and Systems*, 6 (2):147–165, 2010.

- [39] E. Torre, S. Marelli, P. Embrechts, and B. Sudret. Data-driven polynomial chaos expansion for machine learning regression. *Journal of Computational Physics*, 388:601–623, 2019.
- [40] A. H. Seno and M. H. F. Aliabadi. Uncertainty quantification for impact lamination and force estimation in composite structures. *Structural Health Monitoring*, pages 1–15, 2021.
- [41] J. Santiago, M. Claeys-Bruno, and M. Sergent. Construction of space-filling designs using WSP algorithm for high dimensional spaces. *Chemo-metrics and Intelligent Laboratory Systems*, 113:26–31, 2012.
- [42] G. Wang and S. Shan. Review of metamodeling techniques in support of engineering design optimization. *Journal of Mechanical Design*, 129(4):370–380, 2007.
- [43] L. Laurent, R. Le Riche, B. Soulier, and P.-A. Boucard. An overview of gradient-enhanced metamodels with applications. *Archives of Computational Methods in Engineering*, 26(1):61–106, 2019.
- [44] S. Marelli and B. Sudret. UQLab : A framework for uncertainty quantification in MATLAB. In *Proceedings of the 2nd International Conference on Vulnerability and Risk Analysis and Management (ICVRAM 2014)*, pages 2554–2563, Liverpool, United Kingdom, July 2014.
- [45] N. Wiener. The homogeneous chaos. *American Journal of Mathematics*, 60(4):897–936, 1938.
- [46] B. Sudret. *Uncertainty propagation and sensitivity analysis in mechanical models – Contributions to structural reliability and stochastic spectral*

- methods*. Habilitation thesis, Université Blaise Pascal, Clermont-Ferrand 2, 2007.
- [47] R. Askey and J. Wilson. *Some basic hypergeometric orthogonal polynomials that generalize Jacobi polynomials*, volume 319. AMS, Providence, RI, 1985.
- [48] G. Blatman and B. Sudret. Adaptive sparse polynomial chaos expansion based on least angle regression. *Journal of Computational Physics*, 230 (6):2345–2367, 2011.
- [49] D. G. Krige. A statistical approach to some basic mine valuation problems on the Witwatersrand. *Journal of the chemical metallurgical & mining society of South Africa*, 52 (6):119–139, 1951.
- [50] G. Matheron. Kriging or polynomial interpolation procedures? A contribution to polemics in mathematical geology. *Canadian Institute of Mining and Metallurgy Transactions*, 70:240–244, 1967.
- [51] G. Matheron. *The theory of regionalized variables and its applications*. École Nationale des Mines de Paris, France, 1971.
- [52] R. schöbi, B. Sudret, and J. Wiart. Polynomial-chaos-based Kriging. *International Journal for Uncertainty Quantification*, 5 (2):171–193, 2015.
- [53] M. R. Kianifar and F. Campean. Performance evaluation of metamodelling methods for engineering problems: towards a practitioner guide. *Structural and Multidisciplinary Optimization*, 61:159–186, 2020.

- [54] C. Lataniotis, D. Wicaksono, S. Marelli, and B. Sudret. UQLab user manual – Kriging (Gaussian process modeling). Technical report, Chair of Risk, Safety and Uncertainty Quantification, ETH Zurich, Switzerland, 2021. Report # UQLab–V1.4–105.
- [55] B. Iooss. Numerical study of the metamodel validation process. In *Proceedings of the 2009 First International Conference on Advances in System Simulation*, Porto, Portugal, 2009.
- [56] A. El-Bakari, A. Khamlichi, E. Jacquelin, and R. Dkiouak. Assessing impact force localization by using Particle Swarm Optimization. *Journal of Sound and Vibration*, 333 (6):1554–1561, 2014.
- [57] Z. Sharif-Khodaei, M. Ghajari, and M. H. F. Aliabadi. Determination of impact location on composite stiffened panels. *Smart Materials and Structures*, 21 (10):105026, 2012.
- [58] T. A. El-Mihoub, A. Hopgood, L. Nolle, and A. Battersby. Hybrid Genetic Algorithms: A Review. *Engineering Letters*, 13:124–137, 2006.
- [59] P. L. Bartlett, A. Montanari, and A. Rakhlin. Deep learning: a statistical viewpoint. *arXiv (Statistics Theory)*, page 2103.09177, 2021.